An adaptive finite element method for modeling salt diapirism

P. Massimi [a], A. Quarteroni [a,b] and G. Scrofani [a]

[a] *MOX – Dipartimento di Matematica "F. Brioschi", Politecnico di Milano, Via Bonardi 9, 20133 Milano, Italy*
paolo.massimi@mate.polimi.it, giovanni.scrofani@mate.polimi.it

[b] *CMCS (Chair of Modeling and and Scientific Computing) – IACS EPFL , CH–1015 Lausanne, Switzerland*
alfio.quarteroni@epfl.ch

Abstract

Various types of oil traps have been found to be associated with salt domes in subsurface geology. In this paper the diapiric rise of light salt layers through a denser overburden – the surrounding rocks– is modeled assuming that, in a geological time scale, salt and rocks layers behave like Newtonian fluids. A Lagrangian approach is adopted to track the interface between layers, within the framework of a finite element space discretization. An accurate description of large deformations due to salt movement is achieved using a grid adaptation technique based on geometrical refinement. Different geological cases have been simulated in order to describe the behaviour of rocks and estimate the effect on diapiric growth of buoyancy force, differential loading, gravitational gliding and thin–skinned regional extension. Our computational model accounts also for sedimentation and compaction of the overburden.

Key words: Subsurface geology; tectonics; salt diapirism; finite element methods; interface tracking

1 Introduction

Salt (and ductile shale) movement is an important component of sediment deformation in many settings. The dynamical study of salt tectonics has received increasing attention in the past few years. This has been stimulated by the research in the frame of radioactive waste disposal in salt formation [1], and by an increasing interest in modeling the role of halokinesis in controlling the migration and the trapping of hydrocarbons in rapidly subsiding basins [2].

Salt tectonics has become increasingly important in petroleum exploration because various types of traps have been found to be associated with salt domes. This can be explained in view of the very low permeability of the salt with respect to sedimentary rocks and to its viscous rheological behaviour. Indeed, the *anomalous* behaviour of salt with respect to the visco–elasto–plastic rheology of the surrounding rocks yields large deformations in sedimentary basins. Moreover, the seismic properties of salt cannot be investigated in the framework of seismic exploration since, due to the high velocity of the seismic waves in salt, most of the seismic energy is reflected off the top of salt structures. In addition, the high acoustic impedance between sediment and salt often generates many multiples and the flanks of diapirs are generally too steep to be accommodated by the assumption adopted in classical seismic processing.
A better clarification of the mechanisms involved in the geological deformation of salt structures in the basins can provide the geophysicists with a tool for a correct interpretation of seismic data. More precisely, geological models derived from interpreted seismic data could be tested by physical models [3] or numerical modeling. Seismic profiles and drilling demonstrate that salt diapirs feature a broad variety of shapes, that reflect the variety of modes in which salt diapirs interact with their overburden as they grow. Salt diapirs can actively pierce overburden deposited before they start to build up, or they can passively pierce the overburden built down around them. Figure 1 reports images of a diapir obtained by a seismic profile.
A numerical model is a useful tool in order to understand the interaction of the diapirs with the overburden. Salt structures appear to be rising diapirs of light rocks in a denser overburden. The rise of diapirs is caused by a balance between buoyancy and viscous forces.
Thanks to this assumption the diapiric growth can be modeled using the Rayleigh–Taylor theory, describing the gravitational instability of a layered fluid. In this model the basic physical phenomenon of diapirs is explained by the gravitational instability of a lighter salt underlying a denser overburden [4,5,6,7,8]. If the interface between the two layers is perturbed, the underlying low density rock (salt) will move upward due to density inversion. The growth rate of this structures depends on the density and viscosity contrasts as well as on the thickness of the two media. Many numerical simulations have been performed by using high density viscous fluid with Newtonian rheology. However, in order to give a precise description of the causes of salt movement other phenomena different from the buoyancy force such as, gravitational gliding or differential load are taken into account. The originality of this work is mainly based on techniques proposed to describe the diapirs growth, with the introduction of many different boundary conditions and the Lagrangian tracking of the interfaces coupled with a remeshing algorithm. Thanks to different boundary conditions many realistic geological settings can be simulated (thin–skinned regional extension, sedimentation, erosion). The Lagrangian treatment of the interface allows a good geometrical accuracy in the description of the interfaces, while the remeshing mantains a good mesh

quality.

The outline of this work is as follows. In section 2, we derive a mathemati-

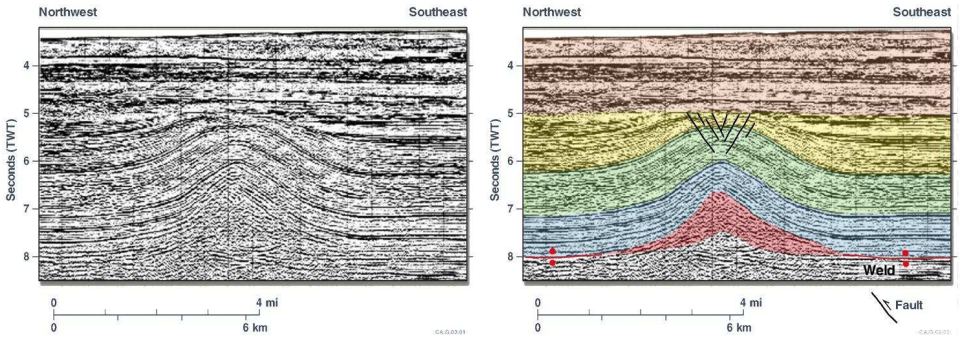

(a) seismic profile (b) geological interpretation

Figure 1. Seismic profile (a) and geological interpretation (b) of a sedimentary basin with a diapir (the red layer).

cal model for the description of diapir evolution based on a Newtonian fluid flow model. A thorough physical explanation is provided, and a dimensional analysis is carried out. In section 3 we describe the numerical method used to simulate the diapirs evolution, the technique used for the mesh generation and the algorithm for tacking the interfaces. In section 4 we report some numerical results on test cases to analyze the diapir behaviour in different situations. Also two realistic simulations of a laboratory experiment and of a geological reconstruction are presented to show the good agreement with experimental data. Finally, in section 5 we consider the coupling of compaction of the overburden with salt evolution.

2 Physical model

In the description of the evolution of sedimentary basins and of the diapiric growth the typical time scales are of the order of millions of years. On this time scale the sedimentary rocks and the halite can be modeled as Newtonian fluids characterized by high viscosity. Thanks to this assumption the description of the diapiric growth can be cast into the framework of the *Rayleigh–Taylor theory* describing the evolution of gravitational instability between two (or several) fluid layers. Further analysis will be performed in the two–dimensional case. In the sequel, we consider sedimentary rocks and halite as incompressible Newtonian fluids having variable density and viscosity, possibly discontinuous.

In this case the Navier–Stokes equations reads:

$$\begin{cases} \rho\dfrac{\partial \mathbf{u}}{\partial t} + \rho(\mathbf{u}\cdot\nabla)\mathbf{u} - \ \mathrm{div}[\mu(\nabla\mathbf{u} + \nabla\mathbf{u}^T)] + \nabla p = \rho\mathbf{g}, \\ \mathrm{div}\mathbf{u} = 0, \end{cases} \tag{1}$$

in $\Omega\times[0,T)$, where Ω is a open set of $\mathbb{R}^n$, $T>0$; ρ is the density, μ the viscosity, $\mathbf{u}$ the velocity field, p the pressure and $\mathbf{g}=(0,-g)^T$ the gravity acceleration. Suitable initial and boundary conditions will be discussed in detail in the following.

2.1 Physical scaling

Let us perform a dimensional analysis on (1) by accounting for typical values of the dynamic parameters involved in the diapiric growth (see table 1). It looks reasonable to choose the following reference values for density and viscosity

$$\tilde{\mu} = 10^{20}\, Pa\cdot s, \qquad \tilde{\rho} = 10^3\,\frac{Kg}{m^3}.$$

Since the time scale is of order of 1 million of years, while the characteristic length of the sedimentary basin is about 1 km, we introduce the following scaling factors for the space and time:

$$T = 1Ma \simeq\ 3.15\cdot 10^{13}s, \qquad L = 1000\,m,$$

while the pressure will be scaled by

$$P = \rho g L = 9.81\cdot 10^6 Pa.$$

Therefore, we consider the following non–dimensional quantities:

$$\tilde{t} = \frac{t}{T}, \qquad \tilde{x} = \frac{x}{L}, \qquad \tilde{p} = \frac{p}{P} \qquad \text{and} \qquad \tilde{\mathbf{u}} = \frac{\mathbf{u}}{U} = \mathbf{u}\frac{T}{L}.$$

Table 1
Geological reference values

Typical values for geological parameters		
	ρ (density)	μ (viscosity)
salt	$2150-2300\ kg/m^3$	$10^{17} Pa\cdot s$
overburden	$2000-2600\ kg/m^3$	$10^{17}-10^{19} Pa\cdot s$
basement	$2300-2600\ kg/m^3$	$10^{19}-10^{23} Pa\cdot s$

Consequently, time and space derivatives will be rescaled as follows:

$$\frac{\partial(\cdot)}{\partial t} = \frac{1}{T}\frac{\partial(\cdot)}{\partial \tilde{t}}, \qquad \nabla(\cdot) = \frac{1}{L}\widetilde{\nabla}(\cdot), \qquad \mathrm{div}\,(\cdot) = \frac{1}{L}\widetilde{\mathrm{div}}\,(\cdot),$$

where $\widetilde{\nabla}$ and $\widetilde{\mathrm{div}}$ are the gradient and divergence operators with respect to the set of non–dimensional variables. Rewriting (1) in terms of the above non-dimensional quantities we obtain

$$\begin{cases} \left(\rho\frac{L}{T^2}\right)\frac{\partial\tilde{\mathbf{u}}}{\partial\tilde{t}} + \left(\rho\frac{L}{T^2}\right)(\tilde{\mathbf{u}}\cdot\widetilde{\nabla})\tilde{\mathbf{u}} - \left(\frac{\bar{\mu}}{LT}\right)\widetilde{\mathrm{div}}\,[\tilde{\mu}(\widetilde{\nabla}\tilde{\mathbf{u}} + \widetilde{\nabla}\tilde{\mathbf{u}}^T)] + (\rho g)\,\widetilde{\nabla}\tilde{p} = \rho\mathbf{g}, \\ \frac{1}{L}\widetilde{\mathrm{div}}\,\tilde{\mathbf{u}} = 0, \end{cases} \tag{2}$$

or, equivalently,

$$\begin{cases} \frac{\partial\tilde{\mathbf{u}}}{\partial\tilde{t}} + (\tilde{\mathbf{u}}\cdot\widetilde{\nabla})\tilde{\mathbf{u}} - \frac{1}{\mathrm{Re}}\widetilde{\mathrm{div}}\,[\tilde{\mu}(\widetilde{\nabla}\tilde{\mathbf{u}} + \widetilde{\nabla}\tilde{\mathbf{u}}^T)] + \frac{1}{\mathrm{Fr}}\widetilde{\nabla}\tilde{p} = \frac{1}{\mathrm{Fr}}\frac{1}{g}\mathbf{g}, \\ \widetilde{\mathrm{div}}\,\tilde{\mathbf{u}} = 0. \end{cases} \tag{3}$$

The *Reynolds* and *Froude* non–dimensional numbers

$$\mathrm{Re} = \frac{\rho\,L^2}{\bar{\mu}\,T}, \qquad \mathrm{Fr} = \frac{L}{T^2\,g}$$

represent, respectively, the ratio between the inertial and viscous forces, and the ratio between buoyancy and inertial forces. Since in our case

$$\mathrm{Re} \simeq 3.174 \cdot 10^{-24}, \qquad \mathrm{Fr} \simeq 1.027 \cdot 10^{-25}$$

the inertial terms can be dropped from the momentum equation of the Navier–Stokes system (3). The evolution of a sedimentary basin can therefore be described by the Stokes system

$$\begin{cases} -\widetilde{\mathrm{div}}\,[\tilde{\mu}(\widetilde{\nabla}\tilde{\mathbf{u}} + \widetilde{\nabla}\tilde{\mathbf{u}}^T)] + F_1\widetilde{\nabla}\tilde{p} = F_2\mathbf{g}, \\ \widetilde{\mathrm{div}}\,\tilde{\mathbf{u}} = 0, \end{cases} \tag{4}$$

where

$$F_1 = \frac{\mathrm{Re}}{\mathrm{Fr}} \simeq 30.481, \qquad F_2 = \frac{1}{g}\frac{\mathrm{Re}}{\mathrm{Fr}} \simeq 3.101.$$

In the sequel the $\sim$ superscripts will be omitted, $\mathbf{u}, p, \ldots$ will denote the non-dimensional quantities and we will indicate by p the value pF_1 and by $\mathbf{g}$ the value $\mathbf{g}F_2$.

Assuming constant rheological properties within each layer we can reduce the time–dependence of the evolution exclusively to the dynamics of the interfaces between layers. In the following analysis only the case with two layers is considered, but it can be easily extended to multi-layered domain. We will suppose the continuity of the velocity field and of the normal part of the stress tensor on the interface Γ_t, separating salt and overburden. An initial configuration Γ_0 is given for the interface. The evolution of each point belonging to the interface is defined as the solution of the kinematic equation

$$\begin{cases} \dfrac{d\boldsymbol{\xi}}{dt} = \mathbf{u}(\boldsymbol{\xi}), \quad \boldsymbol{\xi} \in \Gamma_t \\ \boldsymbol{\xi}(0) = \boldsymbol{\xi}_0 \end{cases} \tag{5}$$

The physical description of the instability of stratified nonhomogeneous fluids (Rayleigh–Taylor instability) can be found in [9]. As a particular case we analyze the evolution of immiscible fluids with different rheological property (density, viscosity).

2.2 Mathematical formulation

According to the analysis of section 2.1 we describe the salt deformation using a Stokes system in $\Omega(t) \subset \mathbb{R}^d$ $(d = 2, 3)$ with moving interface Γ_t. In the sequel the time dependence of the domain and of its boundary is understood. Equations (4) and (5) can be cast in the more general frame of a fluid with variable, possibly discontinuous, density and viscosity. In this context the interface Γ_t (see fig. 2), separating Ω^+ and Ω^- is characterized as the loci of discontinuity of the density ρ. So our model for diapiric growth can be formulated as follows in Ω, for any $t > 0$:

$$\begin{cases} -\text{div } \mathbf{T}(\mu, \mathbf{u}) + \nabla p = \rho \mathbf{g} \qquad \text{in } \Omega, \\ \text{div } \mathbf{u} = 0 \qquad \text{in } \Omega, \\ \dfrac{\partial \rho}{\partial t} + \mathbf{u} \cdot \nabla \rho = 0, \qquad \text{in } \Omega, \\ \mathbf{u} = \mathbf{0} \qquad \text{on } \Gamma_1, \\ \mathbf{u} \cdot \mathbf{n}_2 = 0, \quad (\mathbf{T} - p\mathbf{I})\, \mathbf{n}_2 \cdot \mathbf{t}_2 = 0 \quad \text{on } \Gamma_2, \\ (\mathbf{T} - p\mathbf{I})\mathbf{n}_3 = -p_e \mathbf{n}_3 \quad \text{on } \Gamma_3, \\ \rho|_{t=0} = \rho_0 \qquad \text{in } \Omega_0, \end{cases} \tag{6}$$

where $\Omega = \overset{\circ}{\overline{\Omega^+ \cup \Omega^-}}$, $\partial\Omega = \Gamma_1 \cup \Gamma_2 \cup \Gamma_3$, $\Omega_0 = \Omega(0)$, $\mathbf{T}(\mu, \mathbf{u}) = \mu(\nabla \mathbf{u} + \nabla \mathbf{u}^T)$ is the viscous stress tensor, $\mathbf{I}$ is the identity tensor, $p_e : \Omega \to \mathbb{R}$ (external

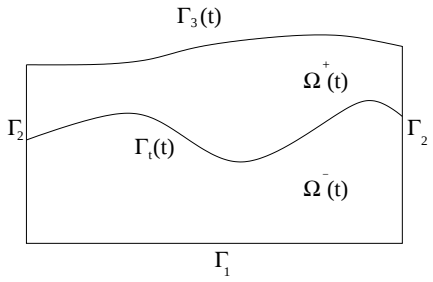

Figure 2. Computational domain

pressure) is a given function, $\mathbf{n}_i$ and $\mathbf{t}_i$ are respectively the unit outward normal and tangent to Γ_i. Free surface boundary condition is assigned on Γ_3.

2.2.1 A Priori estimates

The theory of characteristics applied to the mass conservation equations under the incompressibility assumption implies that, if $\rho_o(\mathbf{x})$ is such that $0 < \alpha \leq \rho_o(\mathbf{x}) \leq \beta$, $\forall \mathbf{x} \in \Omega_0$, then it holds that $0 < \alpha \leq \rho(\mathbf{x}, t) \leq \beta$ for any $t > 0, \mathbf{x} \in \Omega$.

Multiplying the mass transport equation $(6)_3$ by ρ and integrating over Ω we obtain

$$\frac{1}{2}\int_\Omega \frac{\partial \rho^2}{\partial t}\, d\Omega + \frac{1}{2}\int_\Omega \mathbf{u}\cdot\nabla\rho^2\, d\Omega = 0,$$

which, integrating by parts, becomes:

$$\frac{1}{2}\int_\Omega \frac{\partial \rho^2}{\partial t}\, d\Omega + \frac{1}{2}\int_{\Gamma_3} \rho^2\mathbf{u}\cdot\mathbf{n}\, d\gamma = 0, \tag{7}$$

where the flow incompressibility and the boundary conditions $(6)_{4,5}$ on Γ_1 and Γ_2 have been used.

We recall that the Reynolds' Transport Theorem, states:

$$\int_\Omega \frac{\partial \rho^2}{\partial t}\, d\Omega = \frac{d}{dt}\int_\Omega \rho^2\, d\Omega - \int_{\partial\Omega} \rho^2\mathbf{w}\cdot\mathbf{n}\, d\gamma, \tag{8}$$

where $\mathbf{w}$ is the velocity of the moving boundary $\partial\Omega$.

Using this theorem, (7) becomes:

$$\frac{d}{dt}\int_\Omega \rho^2\, d\Omega + \int_{\partial\Omega} \rho^2(\mathbf{u}-\mathbf{w})\cdot\mathbf{n}\, d\gamma = 0.$$

Thanks to the Lagrangian tracking we have the kinematic condition $\mathbf{w}\cdot\mathbf{n} = \mathbf{u}\cdot\mathbf{n}$

on $\partial\Omega$, thus

$$\frac{d}{dt}\int_\Omega \rho^2\, d\Omega = 0,$$

that is

$$\|\rho(\cdot,t)\|_{L^2(\Omega)} = \|\rho_0\|_{L^2(\Omega_0)},\ \forall t > 0. \tag{9}$$

On the other hand, multiplying the momentum equation $(6)_1$ by $\mathbf{u} \in H^1_{0,\Gamma_D}$, where Γ_D is the portion of $\partial\Omega$ on which Dirichlet boundary conditions are prescribed, and integrating over Ω we obtain

$$\int_\Omega \nabla\mathbf{u} : \mathbf{T}\, d\Omega = \int_\Omega \mathbf{u}\cdot(\rho\mathbf{g})\, d\Omega + \int_{\Gamma_3} p_e\mathbf{n}\cdot\mathbf{u}\, d\gamma$$

where the incompressibility and the boundary conditions of problem (6) have been used. Using the Schwarz inequality we obtain

$$||\nabla\mathbf{u}||^2_{L^2(\Omega)} \leq \frac{1}{\mu}\left[||\mathbf{g}||_{L^\infty(\Omega)}\,||\rho||_{L^2(\Omega)}\,||\mathbf{u}||_{L^2(\Omega)} + ||p_e||_{L^2(\Gamma_3)}\,||\mathbf{u}||_{L^2(\Gamma_3)}\right],$$

Thanks to the trace theorem (see [10]) and to (9) we have

$$||\nabla\mathbf{u}||^2_{L^2(\Omega)} \leq \frac{1}{\mu}\left[||\mathbf{g}||_{L^\infty(\Omega)}\,||\rho_0||_{L^2(\Omega_0)} + \widetilde{C}\,||p_e||_{L^2(\Gamma_3)}\right]||\mathbf{u}||_{H^1_{0,\Gamma_D}}.$$

Then $||\mathbf{u}||_{H^1_{0,\Gamma_D}} \leq C\,||\nabla\mathbf{u}||_{L^2(\Omega)}$ due to Poincaré's inequality, and therefore we deduce

$$||\nabla\mathbf{u}||_{L^2(\Omega)} \leq \frac{C}{\mu}\left[||\mathbf{g}||_{L^\infty(\Omega)}\,||\rho_0||_{L^2(\Omega_0)} + \widetilde{C}\,||p_e||_{L^2(\Gamma_3)}\right]$$

for a suitable constant $C > 0$.

2.2.2 Numerical scheme

As already noted, to model the diapirs growth, we are interested in the particular case in which the initial function $\rho_0(\mathbf{x})$ is positive and discontinuous. Considering the fluid immiscible, the problem of advection of density and viscosity is equivalent to finding the evolution of the moving boundary Γ_t. At the initial time $t = 0$, the density is piecewise constant and assumes two positive values characterizing the distinct phases of the flow,

$$\rho(\mathbf{x},0) = \rho_0(\mathbf{x}) = \begin{cases} \rho_+,\ \mathbf{x}\in\Omega^+(0) \\ \rho_-,\ \mathbf{x}\in\Omega^-(0) \end{cases},\ \rho_+ > \rho_- > 0 \tag{10}$$

In this case, the condition for density is equivalent to specifying the interface Γ_t that separates the two subdomains $\Omega^+(0)$ and $\Omega^-(0)$ initially occupied by the different fluids. We assume that the viscosity can be determined as a function of the density, $\mu = \mu(\rho)$ (see [11]). In particular, since each material particle has an associated viscosity, μ should satisfy the convection equation $\mu_t + \mathbf{u} \cdot \nabla \mu = 0$. If $\mu = \mu(\rho)$ this equation is satisfied when $\rho_t + \mathrm{div}(\rho \mathbf{u}) = 0$ and the fluid is incompressible. The well–posedness of this problem has been studied by Antontsev [12].
We propose a split algorithm for the solution of problem (6): at every time–step t^n, first we compute the velocity field solving the Stokes problem, then we track the interface Γ_t to update its position:

$$\Gamma_t^n \longrightarrow [\Omega^+, \Omega^-]^n \longrightarrow \rho_+^n,\ \rho_-^n \longrightarrow \overline{\Omega^n} = \overline{[\Omega^+]^n} \cup \overline{[\Omega^-]^n} \cup \Gamma_t^n$$

$$\longrightarrow \{\text{Stokes } (\Omega^n) \longrightarrow \mathbf{u}^n\} \longrightarrow \left\{\text{Tracking } (\Gamma_t^n, \mathbf{u}^n) \longrightarrow \Gamma_t^{n+1}\right\}$$

where by Stokes (Ω^n) we mean the global weak solution on the whole domain described in the next section and by Tracking $(\Gamma_t^n, \mathbf{u}^n)$ we mean the solution of problem (5).

2.3 Weak formulation of the global Stokes problem

We assume that $\mathbf{g} \in (L^2(\Omega))^2$, $\mu \in L^2(\Omega)$, $\rho \in L^2(\Omega)$, $p_e \in L^2(\Gamma_3)$ be some given functions. In order to derive the weak form of $(6)_1$ we choose the test function space

$$V = \left\{\mathbf{v} \in [H^1(\Omega)]^2 : \mathbf{v}_{|\Gamma_1} = 0,\ \mathbf{v} \cdot \mathbf{n}_{|\Gamma_2} = 0\right\},$$

so, the weak form of $(6)_1$ is:

$$\int_\Omega \mu \frac{\nabla \mathbf{u} + \nabla \mathbf{u}^T}{2} : \nabla \mathbf{v}\, d\Omega - \int_\Omega p \mathrm{div}\, \mathbf{v}\, d\Omega = \int_\Omega \rho \mathbf{g} \cdot \mathbf{v}\, d\Omega + \int_{\partial\Omega} (\mathbf{T} - p\mathbf{I})\, \mathbf{n} \cdot \mathbf{v} d\gamma, \quad \forall \mathbf{v} \in V \tag{11}$$

Since $\mathbf{v} \cdot \mathbf{n} = 0$ on $\Gamma_1 \cup \Gamma_2$, the boundaries term reduces to an interface on Γ_3, thus, owing the boundary conditions therein we have $\int_{\Gamma_3} (\mathbf{T} - p\mathbf{I})\, \mathbf{n} \cdot \mathbf{v} d\gamma = \int_{\Gamma_3} p_e \mathbf{n} \cdot \mathbf{v} d\gamma$. In a similar way, choosing a test function $\psi \in Q = L^2(\Omega)$, the weak form of $(6)_2$ becomes:

$$\int_\Omega q\, \mathrm{div}\, \mathbf{u}\, d\Omega = 0. \tag{12}$$

We can rewrite problem $(6)_{1-2}$ in the following form:

$$\begin{cases} \text{find } \mathbf{u} \in V \ , \ \ p \in Q \ : \\ a(\mathbf{u},\mathbf{v}) + b(\mathbf{v},p) = (\rho\mathbf{g},\mathbf{v})_{L^2(\Omega)} - (p_e\mathbf{n},\mathbf{v})_{L^2(\Gamma_3)} \ \forall \mathbf{v} \in V, \\ b(\mathbf{u},q) = 0 \qquad\qquad\qquad\qquad\qquad\qquad\qquad \forall q \in Q, \end{cases} \tag{13}$$

where $(\cdot,\cdot)_{L^2(\Omega)}$ denotes the scalar product in $L^2(\Omega)$, $(\cdot,\cdot)_{L^2(\Gamma_3)}$ that on $L^2(\Gamma_3)$, while the bilinear forms $a : V \times V \to \mathbb{R}$ and $b : V \times Q \to \mathbb{R}$ are defined by:

$$a(\mathbf{u},\mathbf{v}) = \int_\Omega \mu \frac{\nabla\mathbf{u} + \nabla\mathbf{u}^T}{2} : \nabla\mathbf{v} \, d\Omega, \quad b(\mathbf{u},q) = -\int_\Omega q \, \mathrm{div}\, \mathbf{u} \, d\Omega. \tag{14}$$

Existence and uniqueness of the solution of (13) holds if the continuous bilinear form $a(\cdot,\cdot)$ is coercive on $V^0 = \{\mathbf{v} \in V : b(\mathbf{v},q) = 0, \forall q \in Q\}$, if $b(\cdot,\cdot)$ is a continuous bilinear form, and if a positive constant β exists such that $\forall q \in Q, \exists \mathbf{v} \in V : b(\mathbf{v},q) \geq \beta \, ||\mathbf{v}||_{[H^1(\Omega)]^2} \, ||q||_{L^2(\Omega)}$ (see [13] or [10]).

2.3.1 Numerical approximation of the Stokes equations

We introduce two families of finite dimensional subspace $V_h \subset V$ and $Q_h \subset Q$ depending on h (where h is the grid parameter). Then, we approximate (13) with the discrete problem

$$\begin{cases} \text{find } \mathbf{u}_h \in V_h \ , \ \ p_h \in Q_h \ : \\ a(\mathbf{u}_h,\mathbf{v}_h) + b(\mathbf{v}_h,p_h) = (\rho\mathbf{g},\mathbf{v}_h)_{L^2(\Omega)} - (p_e\mathbf{n},\mathbf{v}_h)_{L^2(\Gamma_3)} \ \forall \mathbf{v}_h \in V_h \\ b(\mathbf{u}_h,q_h) = 0 \qquad\qquad\qquad\qquad\qquad\qquad\qquad \forall q_h \in Q_h. \end{cases} \tag{15}$$

We denote by N_h and K_h the dimension of V_h and Q_h, respectively, and by $\{\boldsymbol{\phi}_j : j = 1, \ldots N_h\}$ and $\{\psi_l : l = 1, \ldots K_h\}$ the basis functions. If we set:

$$\mathbf{u}_h(x) = \sum_{j=1}^{N_h} u_j \boldsymbol{\phi}_j(x), \quad p_h(x) = \sum_{l=1}^{K_h} p_l \psi_l(x) \tag{16}$$

the linear system associated to (15) the following block form:

$$\begin{aligned} A\mathbf{U} + B^T\mathbf{P} &= \mathbf{F} \\ B\mathbf{U} &= \mathbf{0} \end{aligned} \tag{17}$$

where

$$A_{ij} = a(\boldsymbol{\phi}_i,\boldsymbol{\phi}_j), \quad B_{li} = b(\boldsymbol{\phi}_i,\psi_l), \quad F_i = (\mathbf{g},\boldsymbol{\phi}_i)_{L^2(\Omega)} - (p_e\mathbf{n},\boldsymbol{\phi}_i)_{L^2(\Gamma_3)}. \tag{18}$$

A is an $N_h \times N_h$ symmetric and positive definite matrix, while B is a rectangular $K_h \times N_h$ matrix.
We recall that to ensure the existence and the uniqueness for the numerical approximation (13) the following inf–sup condition has to be satisfied (see [13] or [10]):

$$\inf_{q_h \in Q_h, q_h \neq 0} \sup_{\mathbf{v}_h \in V_h, \mathbf{v}_h \neq 0} \frac{b(\mathbf{v}_h, q_h)}{||\mathbf{v}_h||_{[H^1(\Omega)]^2} ||q_h||_{L^2(\Omega)}} \geq \beta \tag{19}$$

where β is a positive constant. Using an algebraic argument it can be easily shown that the above condition holds if, and only if, $\ker(\mathrm{B}^{\mathrm{T}}) = \mathbf{0}$.
In the simulations presented in the next sections we will adopt $\mathbb{P}_1$ finite elements for the pressure and $\mathbb{P}_2$ finite elements for each component of the velocity field.

3 Numerical approximation of the interfaces

Numerical simulations have been performed in a more general context, taking into account n layers and possibly variable rheological properties in each layer. Experimental data and numerical simulations show that very large deformations occur in the salt and in the overburden during the diapiric rise. An accurate approximation of the interface is therefore crucial in order to faithfully describe very distorted shapes and to follow the geometry evolution. The closed curves (e.g. the curve C in Figure 3) describe internal subdomains, while the open curves describe subdomains that touch the boundaries (like curves A and B in Figure 3(a)). All interfaces are described by piecewise lin-

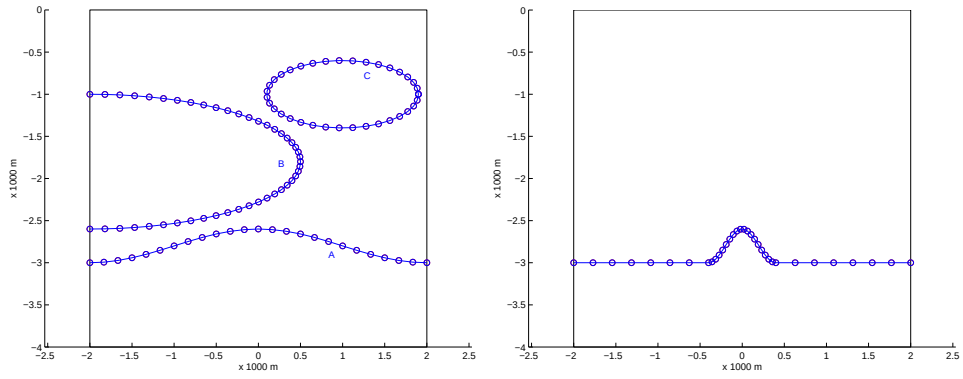

Figure 3. Piecewise linear interface curves (a) and non–uniform spaced nodes(b).

ear approximation and the number of nodes can be locally increased in order to enhance resolution in the description of complex shapes. On the other hand the computational cost can be lowered by using fewer points where the interface features a small curvature (e.g. Figure 3(b)).

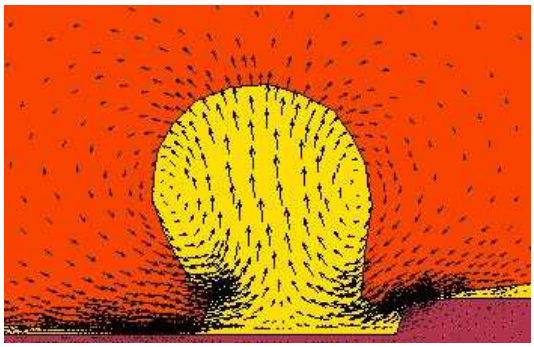

Figure 4. An example of the computed velocity field

3.1 Interface tracking

To update the geometry, a Lagrangian transport of the interface is performed at each time step. The motion of the interface is governed by system (5) where $\boldsymbol{\xi}$ is the position of a generic interface point and $\mathbf{u}$ is the velocity field computed solving problem (15). Figure 4 shows an example of the computed velocity field. To solve the differential equation (5) we use an explicit Euler scheme. A refinement/derefinement criterion is then applied to the tracked interface. Let A_t and B_t be two adjacent points of the interface at the time t and l_t be the length of the segment $\overline{A_t B_t}$. (See figure 5). When these points are moved respectively to $A_{t+\triangle t}$ and $B_{t+\triangle t}$ according to the velocity field, their distance is $l_{t+\triangle t}$, and we can define, for each segment, the following ratio:

$$r = \frac{l_{t+\triangle t}}{l_t}.$$

If $r > 1$ the length of the segment is increasing and this is a potential source of inaccuracy in the description of the interface. A simple remedy to avoid excessive elongation of the segment consists in choosing a proper reference length $\bar{l}_r$ for refinement and adding a point C_t between A_t and B_t if $l_{t+\triangle t} > \bar{l}_r$. With this aim, we consider the middle point C_t of the segment and track its position using the current velocity field. Then the segment $\overline{A_{t+\triangle t} B_{t+\triangle t}}$ is replaced by the two segments $\overline{A_{t+\triangle t} C_{t+\triangle t}}$ and $\overline{C_{t+\triangle t} B_{t+\triangle t}}$. This procedure is not very expensive and far more accurate than splitting $\overline{A_{t+\triangle t} B_{t+\triangle t}}$ into $\overline{A_{t+\triangle t} M}$ and $\overline{M B_{t+\triangle t}}$, where M is the middle point of $\overline{A_{t+\triangle t} B_{t+\triangle t}}$.
If $r < 1$ the length of the segment is decreasing and this could lead to computational inefficiency where too many points close up. As done for the refinement, we can choose a reference length $\bar{l}_d$ for the de–refinement. If $l_{t+\triangle t} < \bar{l}_d$ the point $B_{t+\triangle t}$ collapses to $A_{t+\triangle t}$, so that segment $\overline{A_{t+\triangle t} B_{t+\triangle t}}$ is removed. These refinement/derefinement procedures provide better results by using variable reference lengths $\bar{l}_r$ and $\bar{l}_d$. In the code used for the numerical validation, we scale the reference lengths by a non-dimensional factor λ taking into account the local curvature of the interface. In Figures 7 and 8 examples of the effects of the refinement on the interfaces evolution are illustrated.

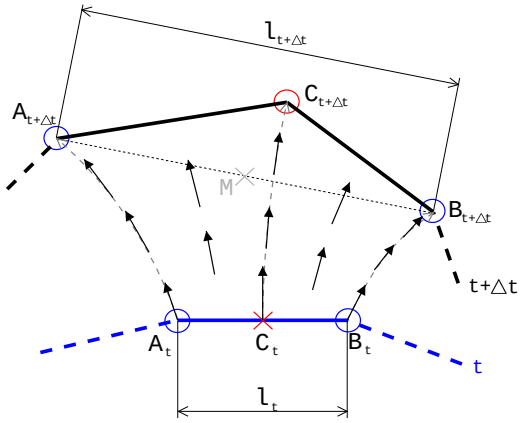

Figure 5. Interface refinement

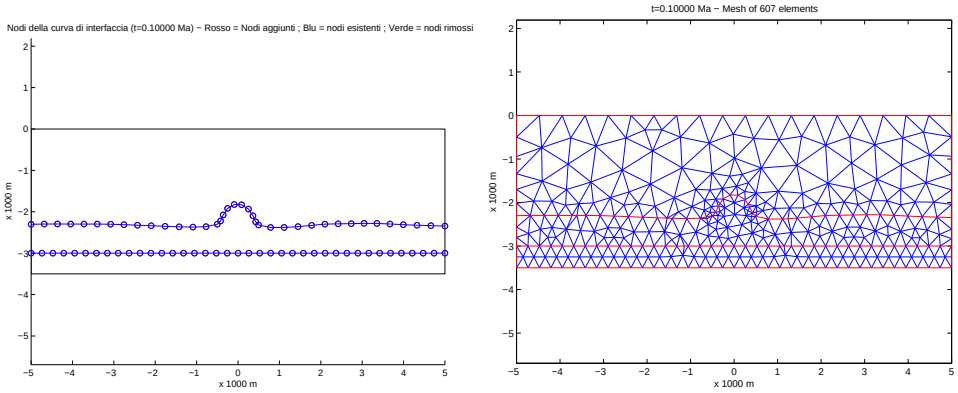

(a) initial curve (b) initial mesh

Figure 6. Initial discretization of the interface and of the computational domain

3.2 Mesh generation and motion

In our simulations we have used an unstructured triangular mesh suitable for complex geometries. A great flexibility in reproducing the motion of the interface is thus obtained. The flowchart of the algorithm is shown in Figure 9. At the first time step an initial mesh is generated by a *constrained Delaunay* algorithm, taking into account the boundaries of the domain and the interfaces among the different layers. This procedures generates mesh element of " high quality". The following quantity

$$q_T = \frac{4\sqrt{3}|T|}{h_{1,T}^2 + h_{2,T}^2 + h_{3,T}^2}, \quad q = \min_T q_T,$$

where $|T|$ is the area while $h_{1,T}$,$h_{2,T}$,$h_{3,T}$ the side lengths, is an assessment of the quality of a triangle. Indeed q_T varies between 0 and 1 and $q_T = 1$ if

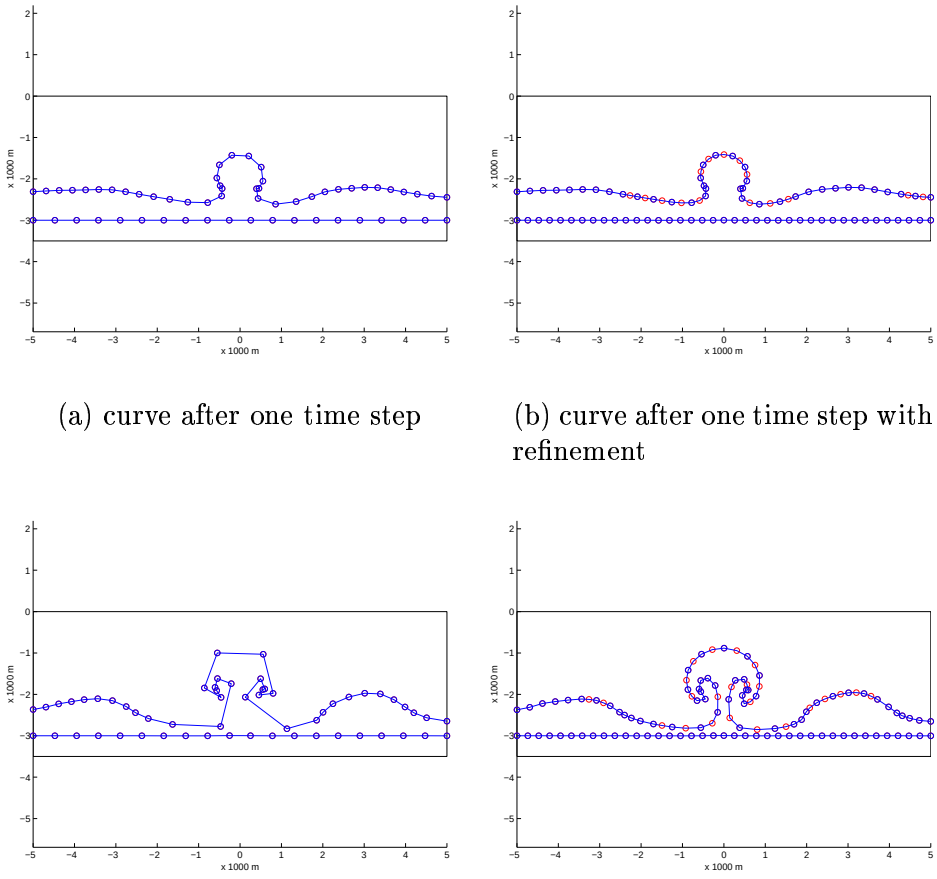

(a) curve after one time step

(b) curve after one time step with refinement

(c) curve after two time steps

(d) curve after two time steps with refinement

Figure 7. Interface evolution without refinement ((a) and (c)) and with refinement ((b) and (d))

$h_{1,T} = h_{2,T} = h_{3,T}$ while q_T approaches 0 when the triangle is distorted so that its vertices are aligned (up to machine precision). The Stokes solver is thus run on this initial mesh to produce the velocity field used to move the mesh in a Lagrangian way. The Lagrangian tracking is performed using the same Euler scheme already used for tracking the interfaces. Thus we obtain a tracked mesh, whose elements usually have a lower quality than the initial ones. A minimum quality threshold $\bar{q}$ is chosen (for example $\bar{q} \simeq 0.5$) to decide whether the mesh has an acceptable quality or not. If $q \geq \bar{q}$ the mesh is accepted and we compute a new velocity field, otherwise a quality recover is attempted by moving the nodes that don't belong to the interfaces or to the boundary toward the center of mass of the corresponding patch [14] (see Figure 10). If the obtained mesh fulfills the quality requirements, then it is used for the next cycle, otherwise a new grid is generated by the *constrained Delaunay* algorithm. Notice that in two space dimensions the remeshing technique is not very expensive, so this scheme is very efficient.

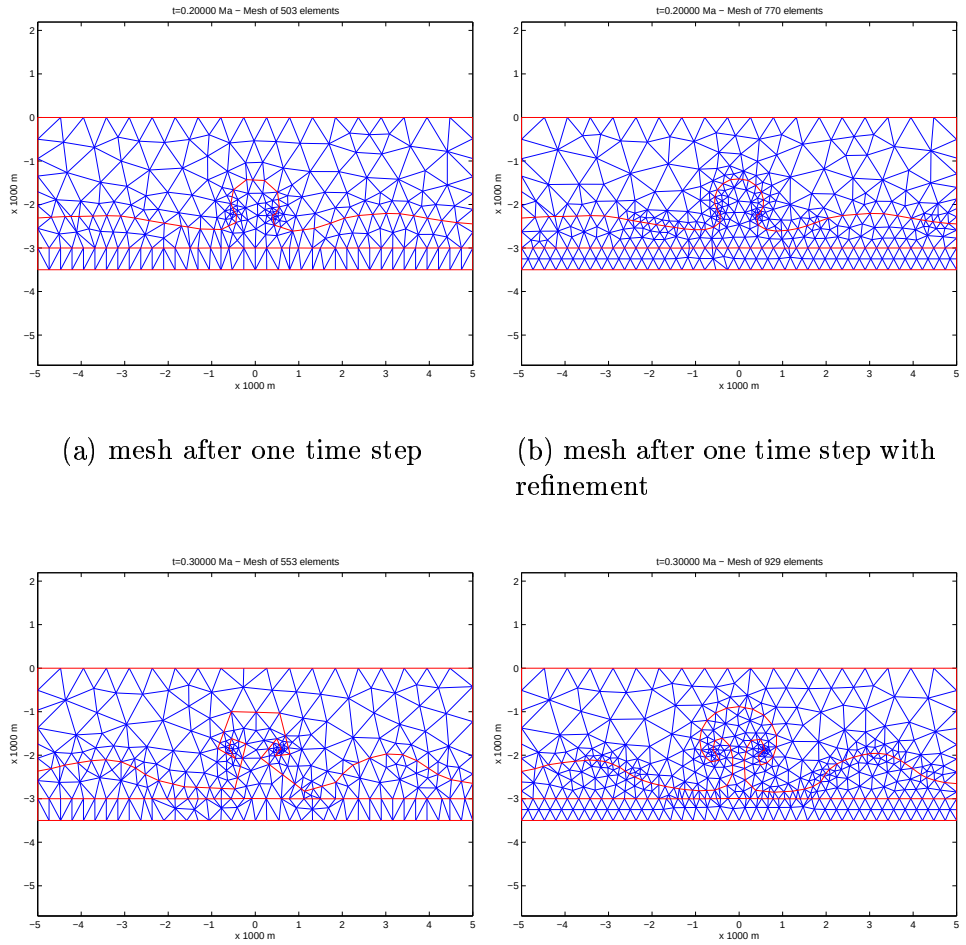

(a) mesh after one time step

(b) mesh after one time step with refinement

(c) mesh after two time steps

(d) mesh after two time steps with refinement

Figure 8. Mesh evolution without refinement ((a) and (c)) and with refinement ((b) and (d))

4 Results of numerical simulation of diapir growth

A density–depth relation and a viscosity–depth relation can be assigned to each layer in order to simulate compaction effects of the overburden. The influence of temperature, lithostatic pressure and composition of sedimentary rocks on their equivalent viscosity components may be taken into account as well.

We consider now some models representing standard geological configurations. The simulations can be done by considering a multilayer computational domain. However, in order to highlight the most relevant physical effects in the considered test cases we have adopted only a three layered domain, in which the first layer represents the basement, the second one the salt and the third

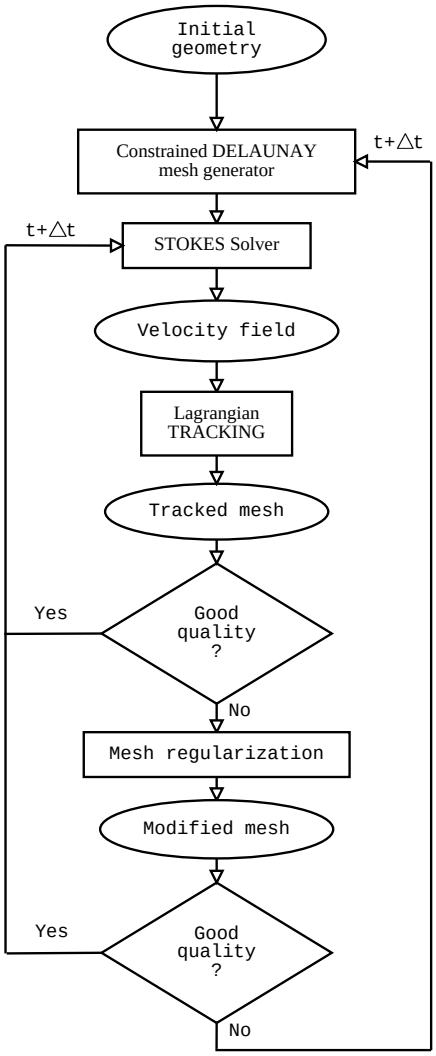

Figure 9. Flowchart for mesh generation, solver and mesh adaption

one the overburden.
In Model A (Figure 11) numerical simulation with constant rheological parameters has been performed using $\rho_b = 2200kg/m^3$ and $\mu_b = 1 \cdot 10^{20} Pa \cdot s$) for the basement, $\rho_s = 2200kg/m^3$, and $\mu_s = 1 \cdot 10^{17} Pa \cdot s$ for the salt, $\rho_o = 2600kg/m^3$ and $\mu_o = 4 \cdot 10^{19} Pa \cdot s$ for the overburden.
The initial disturbance is achieved by a distortion of the layer interface. In the first stage of the evolution the amplitude of the layer interface grows exponentially according to linear Rayleigh–Taylor theory.
When the diapir swells to form a *bulb*, the ascent velocity remains constant as expected from Stokes flow. However the fact that most of natural salt diapirs deviate from spherical shapes indicates that the resistance of the overburden and the buoyancy driving force rarely balance. This balance can be upset in two ways. If the overburden viscosity increases with depth (model B), a diapir

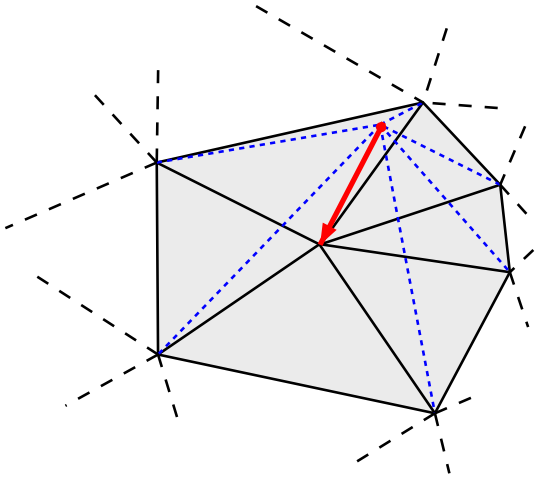

Figure 10. Regularization on a patch of triangles

experiences lower resistance the higher it rises. This leads to accelerated rise and results in elongated shape (Figure 12). So we deduce that the change of the overburden viscosity with depth controls the ratio between the horizontal and the vertical component of the structural development. Alternatively, an increase in overburden density with depth (model C) delays salt ascent because of the density contrast between diapir and overburden, and thus the buoyancy force decrease as the salt ascends (Figure 13). Moreover, if the salt diapir reaches a level with equivalent density, it intrudes horizontally into the overburden and stops its vertical motion.

Model D is an example of the initiation of salt movement by a differential loading by its overburden. It demonstrates the importance of lateral pressure gradient in driving salt flow. In this model the salt top is initially flat (Figure 14). If there is no perturbation the salt layer can subside to huge depth without any movement despite the inverse density stratification. However a lateral variation in loading upsets this unstable equilibrium. Also a small differential loading can be the cause of the development of the instability. The asymmetry results partly from the differential loading, but mainly from asymmetric flow of salt to the base of diapir. This phenomenon is equivalent to a tilted salt layer beneath a homogeneous overburden.

In model E a salt layer embedded in a sedimentary basin environment is shown. Salt flow is completely driven by a lithostatic pressure field. A horizontal pressure gradient activates the instability. The model simulations (figure 15) demonstrate the interaction of salt layer thickness and the layer curvature with the formation and position of salt concentration by flow.

In Model F we have tested the numerical code within realistic situations. It reproduces an analogic experiment (Ge et al.,(1997)]), meant to demostrate how basement steps and prograding sediments control diapir location

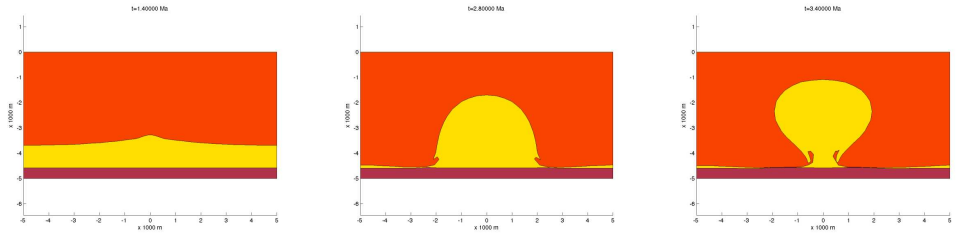

(a) t=1.4 Ma (b) t=2.8 Ma (c) t=3.4 Ma

Figure 11. Model A: the following values are referred to the basement, the salt and the overburden $\rho_b = 2200kg/m^3$,$\mu_b = 1 \cdot 10^{20} Pa \cdot s$, $\rho_s = 2200kg/m^3$, $\mu_s = 1 \cdot 10^{17} Pa \cdot s$, $\rho_o = 2600kg/m^3$, $\mu_o = 4 \cdot 10^{19} Pa \cdot s$.

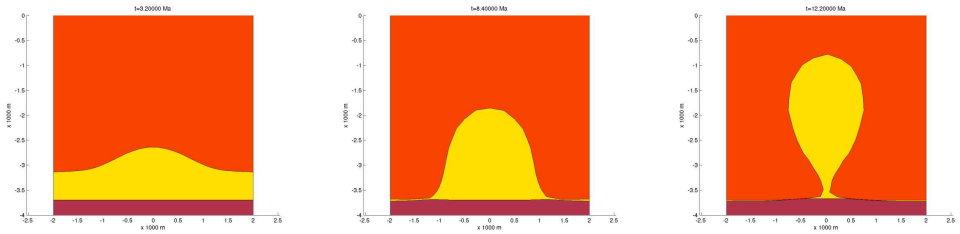

(a) t=3.2 Ma (b) t=8.4 Ma (c) t=12.2 Ma

Figure 12. Model B: the reference value are the same adopted in the previous simulation, the overburden viscosity varies linearly with depth from $10^{17} Pa \cdot s$ (top) to $10^{19} Pa \cdot s$ (bottom)

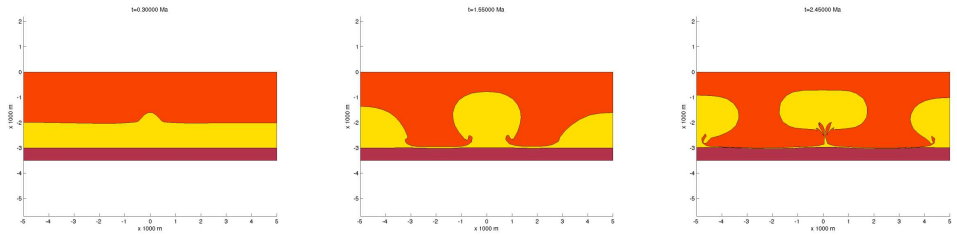

(a) t=0.3 Ma (b) t=1.55 Ma (c) t=2.45 Ma

Figure 13. Model C: the reference value are the same adopted in the previous simulation, the overburden density varies linearly with depth from $2000Kg/m^3$ (top) to $2600Kg/m^3$ (bottom) The salt top does not rise above its level of neutral buoyancy.

5 Compaction

The overburden is a saturated porous media, so its effective density ρ_o can be represented as:

$$\rho_o = (1 - n)\rho_g + n\rho_w \tag{20}$$

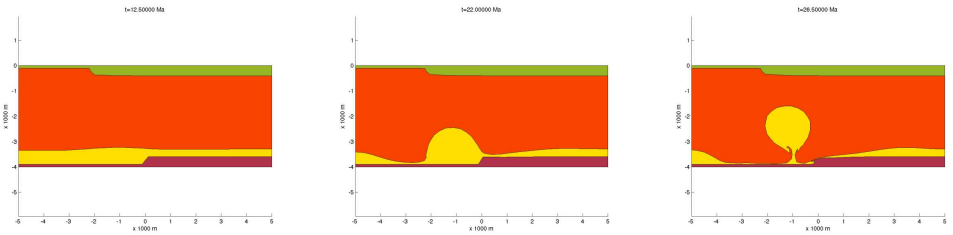

(a) t=12.5 Ma (b) t=22 Ma (c) t=26.5 Ma

Figure 14. Model D: multilayered overburden with lateral variation. The effect of differential loading activates the diapirism.

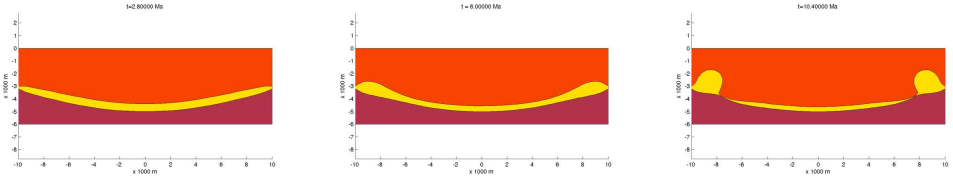

(a) t=2.8 Ma (b) t=6 Ma (c) t=10.4 Ma

Figure 15. Model E: the effect of lithostatic pressure in a sedimentary basins activates the diapirism

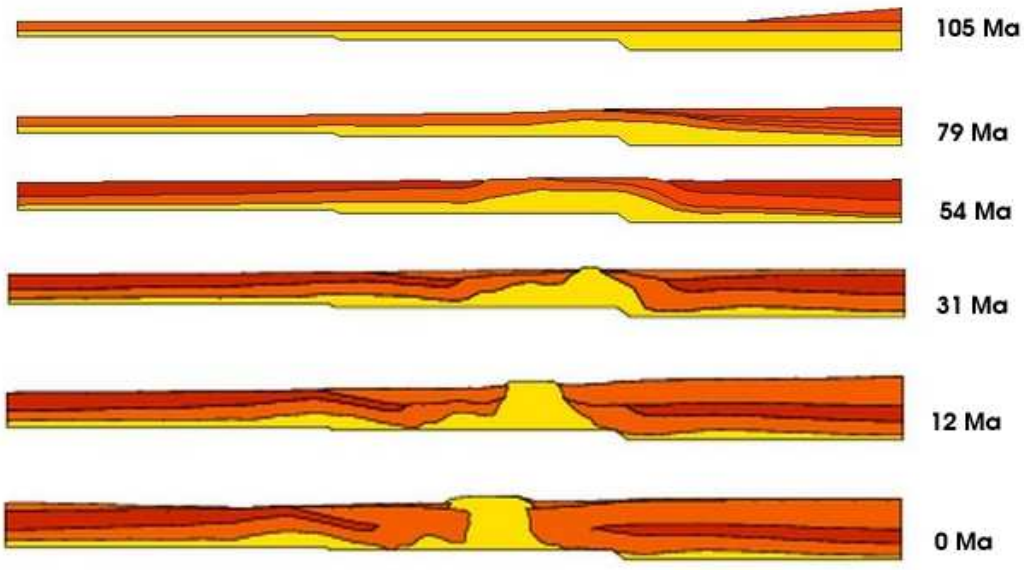

Figure 16. Model F: sedimentary basin with basament steps and progradation

where n is the porosity, ρ_g is the grain density, and ρ_w is the density of water. We recall the Athy's law [15] for porous media:

$$n(z) = n_0 e^{(-cz)} \tag{21}$$

where n_0 is the surface porosity at sea level and z is the sea level depth and c is a dimensional constant [16]. We estimate the effects of compaction due to the gravity force on diapirs evolution. We assume that ρ_g is constant and we neglect the effect of poroelasticity during compaction. Let us start with the mass conservation equations for both the fluid and solid phase in the overburden:

$$\frac{\partial(\rho_w n)}{\partial t} + \text{div } (\rho_w n \, \mathbf{v}_w) = 0, \tag{22}$$

$$\frac{\partial[\rho_g(1-n)]}{\partial t} + \text{div } (\rho_g(1-n)\mathbf{v}_g) = 0, \tag{23}$$

where $\mathbf{v}_w$ and $\mathbf{v}_g$ are respectively the velocity of the water and of the grain. Supposing that the grain density remains constant along streamlines, equation (23) becomes:

$$\text{div } \mathbf{v}_g = \frac{1}{1-n}\frac{Dn}{Dt}. \tag{24}$$

We suppose that $n = n(z)$ is a given function, so the porosity of each point changes due to the deposition of an additional layer. For further details see [17] and [18].
Formally integrating (24) and assuming only vertical compaction we obtain the following problem:

$$\begin{cases} \dfrac{dS}{dz} = \dfrac{\delta n}{1-n} & \text{in } \Omega \subset \mathbb{R}^2 \\ S = 0 & \text{on } \Gamma_b \end{cases} \tag{25}$$

where S is the vertical displacement and δn is the porosity variation of each layer, Γ_b is the bottom line of the computational domain Ω.
We solve problem (25) with a stabilized finite element scheme. In particular we approximate S with piecewise linear polynomials and we use SUPG method (see [10]).

In Figure 17 some numerical results of diapiric growth in a sedimentary basin with sedimentation and compaction are shown. We assume constant density of the grains $\rho_g = 2700 kg/m^3$, a given law for porosity (see [19]) and a constant sedimentation rate of $300 m/Ma$. The height of sedimentary basin varies during the evolution and a deformation above the diapir due to compaction occurs.

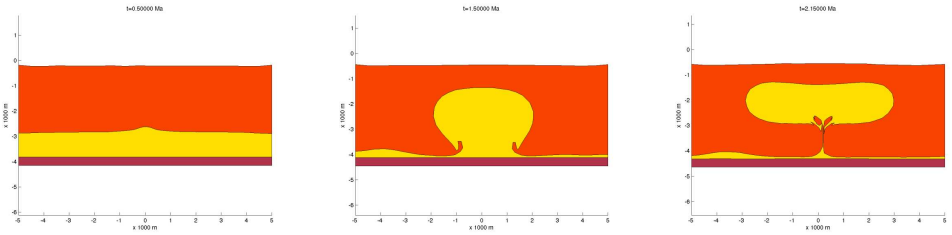

(a) t=0.5 Ma (b) t=1.5 Ma (c) t=2.15 Ma

Figure 17. Evolution of a diapir in a sedimentary basin with constant sedimentation rate and compaction.

6 Conclusions

We developed a two-dimensional Finite–Element code for the simulation of diapirs intrusion into an arbitrary layered overburden with time and depth-dependent properties and time–dependent thickness. We use a split algorithm in which we first solve a Stokes problem by FEM at each time–step and then we carry out the interface tracking with an adaptive grid technique. This program can analyze the influence on salt flow of different conditions such as differential loading due to inhomogeneities in the overburden, the shape of the salt base, subsidence of uplift of the salt base during evolution of sedimentary basin, and increase in density and viscosity due to sedimentation and compaction.

Acknowledgements

We acknowledge Drs P. Ruffo and D. Fragola from ENI E.&P., Professors F. Saleri, L. Formaggia and E. Miglio for their advises and collaboration on this project. This research has been supported by the "HPC on PSM" project in collaboration with ENI, Divisione E.&P. and by the Italian research project Cofin2003-MIUR "Numerical Modeling for Scientific Computing and Advanced Applications".

Appendix

Rayleigh–Taylor instability theory

In this appendix a simplified version of the Rayleigh–Taylor instability model is analyzed. We consider a classic linear instability problem of two semi–infinite inviscid fluids of densities ρ_1 (in the region $z < 0$) and $\rho_2 < \rho_1$ (in the region $z > 0$), separated by a horizontal boundary at $z = 0$. We may consider an interfacial surface tension T. The disturbed flow of the two fluids is assumed to be irrotational so that the velocity potential of the lower fluid is φ_1 and that of the upper fluid is φ_2.
With the interfacial surface elevation $\eta = \eta(x, y, t)$, the perturbed quantities satisfy the following boundary and interfacial conditions:

$$\left(\frac{\partial \varphi_1}{\partial z}, \frac{\partial \varphi_2}{\partial z}\right) \to (0, 0) \qquad \text{for } z \to \mp\infty \tag{.1}$$

$$\frac{\partial \varphi_1}{\partial z} = \frac{\partial \eta}{\partial t}, \ \frac{\partial \varphi_2}{\partial z} = \frac{\partial \eta}{\partial t} \qquad \text{at z} = 0 \tag{.2}$$

$$\rho_1 \left(\frac{\partial \varphi_1}{\partial t} + g\eta\right) = \rho_2 \left(\frac{\partial \varphi_2}{\partial t} + g\eta\right) + T\triangle\eta \ \text{ at } \ z = 0 \tag{.3}$$

where $\triangle$ is the two–dimensional Laplace operator. We analyze the instability problem using the standard normal mode analysis. A typical Fourier component of the interfacial elevation has the form

$$z = \eta(x, y, t) = A \exp\left[i(\boldsymbol{\kappa} \cdot \mathbf{x} - \omega t)\right], \tag{.4}$$

where A is an arbitrary constant, $\mathbf{x} = (x, y)^T$, $\boldsymbol{\kappa} = (k, l)^T$ is the horizontal wavenumber vector and $\omega(k, l)$ is a (possibly complex) frequency. The associated velocity potentials satisfying the boundary conditions (.1) are:

$$\varphi_1 = A_1 \exp\left[i(\boldsymbol{\kappa} \cdot \mathbf{x} - \omega t) + \kappa z\right], \tag{.5}$$

$$\varphi_2 = A_2 \exp\left[i(\boldsymbol{\kappa} \cdot \mathbf{x} - \omega t) - \kappa z\right], \tag{.6}$$

where $\kappa = (k^2 + l^2)^{1/2}$ and the constants A_1 e A_2 can be easily determined, otherwise, conditions (.2) yield:

$$\kappa A_1 = \kappa A_2 = -i\omega A. \tag{.7}$$

From the dynamic boundary condition (.3) we get:

$$\omega^2 = g\kappa \left[\frac{\rho_1 - \rho_2}{\rho_1 + \rho_2} + \frac{T\kappa^2}{g(\rho_1 + \rho_2)} \right]. \tag{.8}$$

This quadratic equation for ω has either real or complex roots. For real roots, there are two waves that propagating with constant amplitude. For complex-conjugate roots the wave mode decays and grows exponentially according to the sign of the imaginary part, positive and negative, respectively. If there exists an exponentially growing mode for some wavenumber (k, l), then the primary flow in *unstable*. One the other hand, the flow is regarded as *stable*. We point out that stability, in this sense, does not mean the decay of all the disturbances as $t \to \infty$, but simply the absence of the growing mode.
We define the horizontal coordinate $\bar{x} = (1/\kappa)(\boldsymbol{\kappa} \cdot \mathbf{x})$ in the direction of the wavenumber vector $\boldsymbol{\kappa}$. Clearly, waves propagate in the direction of increasing $\bar{x}$ with phase velocity $Re(\omega)/\kappa$. Moreover, the quantity of ω/κ depends on k and l, and hence the waves are *dispersive*. Relation (.8) is the so–called *complex dispersion relation* for interfacial waves and gives:

$$\omega = \pm\sqrt{(g\kappa)} \left[\frac{\rho_1 - \rho_2}{\rho_1 + \rho_2} + \frac{T\kappa^2}{g(\rho_1 + \rho_2)} \right]^{1/2}. \tag{.9}$$

These roots are real provided that $g(\rho_1 - \rho_2) + T\kappa^2$ is positive (when $\rho_2 < \rho_1$, the associated modes describe interfacial capillary–gravity waves). When the lighter fluid is beneath the heavier one, the system is unstable for all wave-numbers with

$$\kappa^2 < \frac{g}{T}(\rho_2 - \rho_1).$$

This means that sufficiently long waves are unstable in the range $0 < \kappa < \kappa_c$, where

$$\kappa_c = \left[\frac{g}{T}(\rho_2 - \rho_1) \right]^{1/2}. \tag{.10}$$

On the contrary, the system is stable for any disturbance if $\kappa > \kappa_c$. Thus, the effect of the surface tension is to stabilize a potentially unstable system for all sufficiently large wave-numbers.
In the description of the evolution of salt diapirs we neglect the surface tension (i.e. $T = 0$). In such a case the dispersion relation reduces to

$$\omega^2 = g\kappa \left(\frac{\rho_1 - \rho_2}{\rho_2 + \rho_1} \right). \tag{.11}$$

If $\rho_1 < \rho_2$ the value of ω is purely imaginary and the system is unstable for any frequency. The phase and group velocities of the waves are given by

$$C_p = \frac{\omega}{\kappa} = \pm \left[\frac{g}{\kappa} \left(\frac{\rho_1 - \rho_2}{\rho_2 + \rho_1} \right) \right]^{\frac{1}{2}}, \qquad C_g = \nabla_\kappa \omega \tag{.12}$$

respectively, where $\nabla_\kappa \omega = \nabla \omega \cdot \boldsymbol{\kappa}$ represents the derivative of ω along the direction $\boldsymbol{\kappa}$.

References

[1] S. Zaleski. Numerical simulation of Rayleigh–Taylor instability for single and multiple salt diapirs. *Tectonophysics*, **206** (1992)

[2] C. J. Talbot. Halokinesis and thermal convection *Nature*, **273** (1978)

[3] D.D. Schultz–Ela, M.P.A. Jackson, and B.C. Vendeville. Mechanics of active salt diapirism. *Tectonophysics*, **228** (1993)

[4] A. T. Ismail–Zadeh. Implementation of a three–dimensional hydrodynamic model for evolution of sedimentary basins. *Comput. Math. & Math. Phys.*, **38** (1998)

[5] A. T. Ismail–Zadeh and C. J. Talbot. Dynamic restoration of profiles across diapiric salt structures: numerical approach and its application. *Tectonophysics*, **337** (2001) 23–38

[6] Y. Podladchikov. Numerical analysis of how sedimentation and redistribution of surficial sediments affects salt diapirism. *Tectonophysics*, **226** (1993)

[7] A. Poliakov and Y. Podladchikov. Diapirism and topography. *Geophys. J. Int.*, **109** (1992)

[8] A. Poliakov, Y. Podladchikov, and C. Talbot. Numerical model of complex diapirism. *Tectonophysics*, **228** (1993)

[9] S. Chandrasekhar. *Hydrodinamic and hydromagnetic instability.* Oxford University Press, 1961.

[10] A. Quarteroni and A. Valli. *Numerical Approximation of Partial Differential Equations*. Springer Verlag, Berlin, 1997

[11] P. L. Lions. *Mathematical Topics in Fluid Mechanics*, volume 1: Incompressible Models. Oxford Press, Oxford, U.K., 1996.

[12] S. Antontsev, A. Meirmanov, and B. V. Yurinsky. A free-boundary problem for Stokes equations: classical solutions. *Interfaces Free Bound.*, **2**(4) (2000) 413–424

[13] F. Brezzi. On the existence, uniqueness and approximation of saddle–point problems arising from Lagrange multiplier. *R.A.I.R.O. Anal. Numér.*, **8** (1974) 129–151

[14] P.L. George and H. Borouchaki. *Delaunay triangulation and meshing–application to finite element.* Editions Hermes, Paris, 1998

[15] L. F. Athy. Density, porosity, and compaction of sedimentary rock. *Amer. Ass. Petrol. Geol. Bull.*, **14** (1930) 1–22

[16] C.M. Bethke. A numerical model of compaction–driven grownd water flow and heat transfer and its application to the paleohydrology of intractatonic sedimentary basins. *J. Geophys. Res*, **90** (1985) 6817–6828

[17] D. M. Audet and A. C. Fowler. A mathematical model for compaction in sedimentary basins. *Geophys. J. Int.*, **110** (1992) 577–590

[18] S. X. Yang. *Mathematical modelling of compaction and diagenesis in sedimentary basins.* PhD Thesis, Oxford, 1997.

[19] A. C. Fawler and S. X. Yang. Fast and slow compaction in sedimentary basins. *SIAM J. Appl. Math.*, **59** (1998) 365–385